LIMNOLOGY and OCEANOGRAPHY

ASLO

Limnol. Oceanogr. 69, 2024, 1562–1576

doi: 10.1002/lno.12596

Photosynthetic processes in Antarctic sea ice during the spring melt

Jodi N. Young,[1*] **Susan Rundell**,[1] **Zachary S. Cooper**,[1,a] **Hannah M. Dawson**,[1] **Shelly D. Carpenter**,[1] **Thomas Ryan-Keogh**,[2] **Elden Rowland**,[3] **Erin M. Bertrand**,[3] **Jody W. Deming**[1]

[1]School of Oceanography, University of Washington, Seattle, USA
[2]Southern Ocean Carbon-Climate Observatory, CSIR, Cape Town, South Africa
[3]Department of Biology, Dalhousie University, Halifax, Nova Scotia, Canada

Abstract

High-latitude oceans experience strong seasonality where low light limits photosynthetic activity most of the year. This limitation is pronounced for algae within and underlying sea ice, and these algae are uniquely acclimated to low light levels. During spring melt, however, light intensity and daylength increase drastically, triggering blooms of ice algae that play important roles in carbon cycling and ecosystem productivity. How the algae acclimate to this dynamic and heterogeneous environment is poorly understood. Here, we measured ^{14}C-carbon fixation rates, photophysiology, and ribulose 1,5-bisphosphate carboxylase oxygenase (Rubisco) content of sea-ice algae in coastal waters near the western Antarctic Peninsula during spring, ranging from a low-light-acclimated, bottom community to a light-saturated bloom. Carbon fixation rates by sea-ice algae were similar to other Antarctic sea-ice measurements (2–49 mg C m^{-2} d^{-1}), and there was little phytoplankton biomass in the underlying water at the time of sampling. Net-to-gross ratios of carbon fixation were generally high and showed no relationship with ice type. We found algal photophysiology and Rubisco concentrations varied in relation to the different types of ice, altering the balance between the photochemical and biochemical processes that constrain carbon fixation rates. For algae inhabiting the bottom layers of sea ice, rates of carbon fixation were largely constrained by light availability whereas in surface seawater, interior and rotten/brash ice, carbon fixation rates could be calculated with reasonable accuracy from measurements of Rubisco concentrations. This work provides additional insight and means to evaluate carbon fixation rates as sea ice continues to change in future.

Coastal waters along the western Antarctic Peninsula are highly productive polar ecosystems that are vulnerable to anthropogenic change. Rising temperatures have shortened the duration, extent, and thickness of sea ice, affecting primary productivity (Schofield et al. 2018) primarily through the availability of light (Joy-Warren et al. 2019). Both sea-ice algae and phytoplankton contribute to primary production in this region, filling different ecological and temporal niches over the seasonal cycle (Kvernvik et al. 2021; Jacquemot et al. 2022). Sea-ice algae have their highest rates of production in early spring, often forming visible bands in the bottom layers or within interior gap layers of the ice (Kattner et al. 2004). Over winter, they are thought to be an important food source for zooplankton, particularly juvenile krill (Bernard et al. 2019). Once the ice melts, sea-ice algal biomass is released from the ice and sinks, exporting carbon (Selz et al. 2018). Sea-ice algae can also seed phytoplankton blooms, which become the dominant primary producers during the ice-free summer (van Leeuwe et al. 2022).

How changes in the timing, duration, and structure of sea ice will impact the seasonal bloom dynamics of sea-ice algae, and their contributions to polar ecosystems is uncertain. Data quantifying the current contribution of sea-ice algae to western Antarctic Peninsula primary production are scarce. There are only a few measurements of sea-ice algal primary production along the western Antarctic Peninsula (Selz et al. 2018; van Leeuwe et al. 2022) even though there is an extensive (~ 30 yr) record of phytoplankton primary production

*Correspondence: youngjn@uw.edu

[a]Present address: Institute of Systems Biology, Washington, USA

Additional Supporting Information may be found in the online version of this article.

Author Contribution Statement: JY and SR conceptualized the study, with input from JWD, HD, JY, SR, ZC, SDC collected field samples and processed data. EMB and ER developed mass spectrometry methods for measuring Rubisco and processed Rubisco samples. TRK advised FIRe analysis. All authors contributed to the writing of the manuscript.
JNY and SR contributed equally to this study.

collected as part of the Palmer Long-Term Ecological Research (LTER) program (Palmer Station Antarctica LTER and Waite 2022).

In the polar environment, temperature, light, and nutrients are major environmental factors driving rates of primary production (carbon fixation). Rates of gross carbon fixation depend on the balancing of light-dependent, temperature-independent photochemical reactions with light-independent, temperature-dependent biochemical reactions (Huner et al. 1998). In addition, net primary production and net community production also include rates of respiration of the photosynthetic and whole community, respectively. Studies have shown that respiration rates have greater temperature sensitivity than photosynthesis (Bozzato et al. 2019). High ratios of net-to-gross ratios of photosynthesis observed in polar phytoplankton have been attributed to lower respiration rates at cold temperatures (Goldman et al. 2015). While photosynthesis may be less temperature sensitive than respiration, cold temperatures nevertheless slow the enzymes involved in biochemical rates of photosynthesis, notably the carboxylation enzyme, ribulose 1,5-bisphosphate carboxylase oxygenase (Rubisco), which is already notoriously slow (Tcherkez et al. 2006). There is little evidence for cold adaptation of the Rubisco enzyme, which led Young et al. (2015) to hypothesize that the maximum growth rates of western Antarctic Peninsula phytoplankton were ultimately constrained by the limited concentration of Rubisco that cells could accumulate. Under replete light and nutrients, we hypothesized that gross carbon fixation rates by sea-ice algae are also likely rate-restricted by carboxylation speed and cellular abundance of Rubisco at cold temperatures.

Compared to temperature adaptations, comparatively more is known about the adaptations of algal photosystems to light availability in polar oceans. Polar algae are well acclimated to low-light conditions, requiring less light for maximum growth and saturating photosynthesis, but overall, generally have slower growth rates than their mesophilic counterparts (Lacour et al. 2017). This low-light adaptation is even more pronounced in sea-ice algae, which can easily become high light-stressed (Kvernvik et al. 2020; Lund-Hansen et al. 2020). There is evidence that polar algae maintain a functional photosynthetic apparatus during the polar winter that enables them to quickly take advantage of early increases in light (Strzepek et al. 2019; Hoppe 2022). As light levels increase, polar algae can rapidly increase metabolic rates and acclimate their photophysiology (Sloughter et al. 2019). During high light and long-day lengths during late spring and summer, polar algae have a high capacity for non-photochemical quenching (NPQ) to dissipate excess excitation energy that can damage photosystems (Lacour et al. 2018). Low temperatures have been suggested to be advantageous for high-latitude algae transitioning from light-limited to light-stressed environments, as the cold mitigates NPQ-dissipated heat (Strzepek et al. 2019).

Here we measured rates of primary production (both gross and net photosynthesis) via ^{14}C tracer incubations of sea-ice algae along a transect in the western Antarctic Peninsula during the austral spring in 2019. These rates were compared to primary productivity measurements of phytoplankton from Palmer LTER and to other Antarctic sea-ice algae to better quantify the contribution of sea-ice algae to western Antarctic Peninsula productivity. The mechanism by which sea-ice algae balance temperature-sensitive and light-sensitive mechanisms of photosynthesis during the spring melt was examined. Photophysiology was characterized using active chlorophyll fluorescence as measured by Fast Induction Relaxation (FIRe), and potential carbon fixation rates were estimated from measured Rubisco concentrations and literature-derived kinetics. Photochemically and biochemically derived rates of carbon fixation were compared with our measured primary production via ^{14}C tracer incubations. This comparison revealed underlying mechanisms that limit production during ice melt and highlighted new approaches to calculate rates of primary production. Understanding the complex interactions between photochemical and biochemical processes in sea-ice algal photosynthesis will help to better model primary production within ice-covered regions, particularly as the timing, thickness and duration of the sea-ice cover continue to diminish (Stammerjohn et al. 2008).

Methods

Field sampling

In 2019, ice samples were collected from six stations (Stas. 2–7) along a north–south transect (64.8°S to 67.8°S) of coastal waters near the western Antarctic Peninsula in November and December on board the R/V *Nathaniel B. Palmer* (Fig. 1; Table 1). At Stas. 3, 5, and 7, seawater was also sampled under the ice for chlorophyll *a* (Chl *a*), particulate organic carbon (POC), and major nutrient concentrations. In addition, surface seawater (< 5 m) was collected in 2018 from open-water off Bonaparte Point (Sta. B of the LTER sampling grid, 64.8°S 64.1°W) over 5 d between 08 November and 19 November, for Rubisco quantification (sample collection described in Dawson et al. 2023).

Sample collection

At Stas. 2 and 3, the ice was rotten/brash (water movement and advanced melt had disintegrated the ice structurally) and was collected as small ice pieces from the surface of an ice-seawater slurry via a crane-suspended "personnel basket." At Stas. 4–7, sea ice was cored with a 7.25-cm diameter Mark III Kovacs corer with each core separated by at least 1 m horizontally. Stas. 4 and 7 were rafted ice floes with flooded interior layers and algal samples were collected from interior ice-core layers. Stas. 5 and 6 were on landfast sea ice, where the algae were collected from the bottom of the ice. Seawater samples were collected into acid-cleaned polycarbonate containers.

Samples were shaded from direct sunlight. Either 5 cm or 10 cm of bottom ice or interior ice that were visibly colored

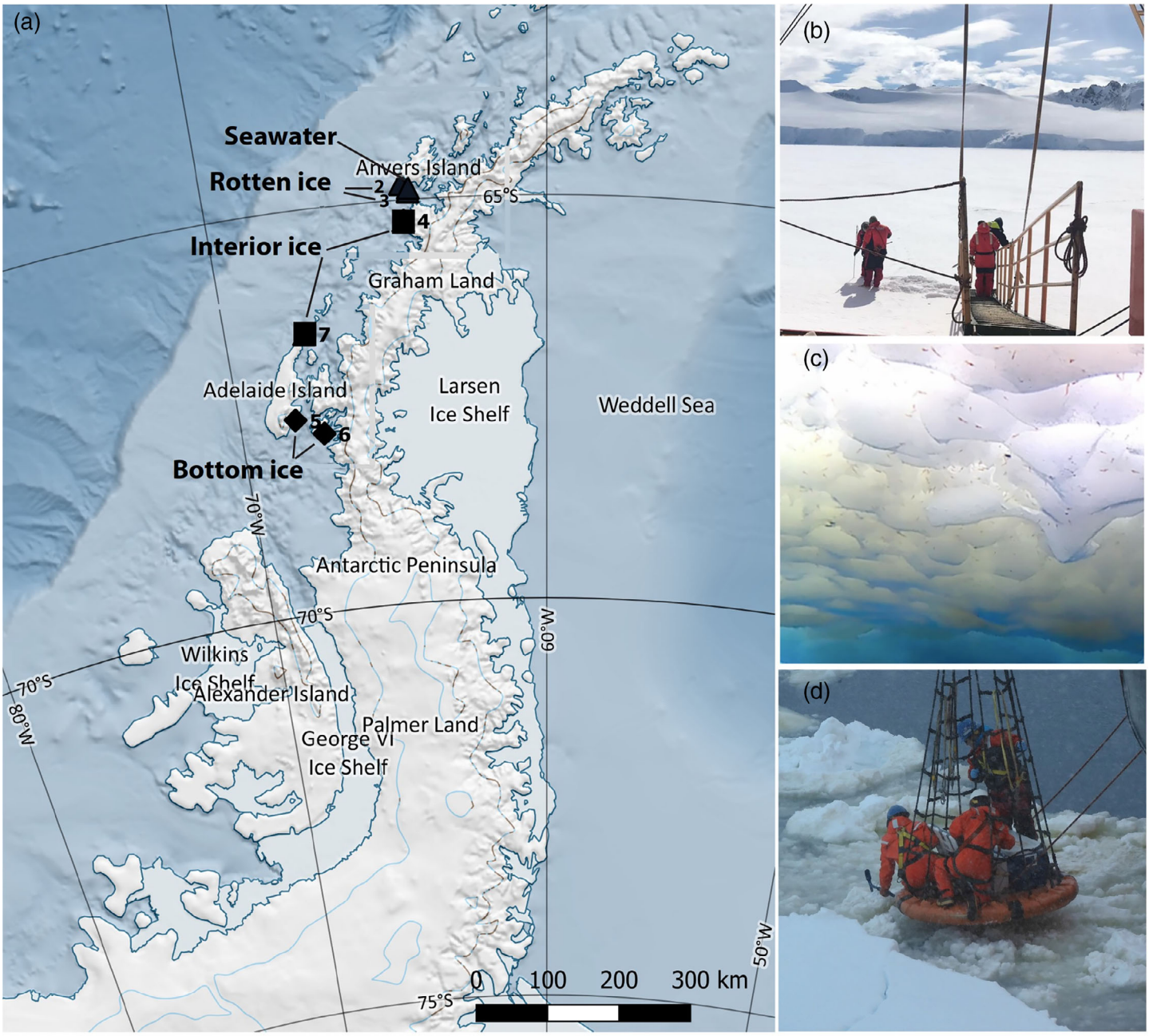

Fig. 1. Sea-ice sampling locations in November 2019 to December 2019 and the seawater sampling location in November 2018 along the western Antarctic Peninsula. (**a**) Map made by QGIS (QGIS.org 2024). Bottom-ice Stas. 5 and 6 (black diamonds), interior-ice Stas. 4 and 7 (black squares) and rotten/brash-ice Stas. 2 and 3 (black triangles). Under-ice seawater sampling location (circle) is hidden behind Sta. 2 triangle. Images taken during sampling at: (**b**) landfast ice at Sta. 5, (**c**) under ice with visible algae and krill at Sta. 4, and (**d**) rotten/brash ice at Sta. 3.

with algae were sectioned with an ethanol-cleaned saw and placed into acid-washed (10% HCl) containers. Each sample consisted of either a single core (for 10-cm sections) or two pooled cores (for 5-cm sections). At each station, duplicate or triplicate samples were collected for each melt treatment (*see* the next section), with the exception of Sta. 4, where samples were pooled and subsampled.

Temperature, salinity, and photosynthetically active radiation (PAR, 400–700 nm) were measured from additional "physical" cores or seawater samples. Temperature was measured with a Therma Waterproof Type T thermometer (ThermoWorks) and conductivity measurements made with both a refractometer and conductivity/TDS meter (EC400S, Apera Instruments). For ice samples, brine volumes and

salinity were calculated from bulk salinity and temperature (Frankenstein and Garner 1967; Cox and Weeks 1986) from direct melts of 5-cm sections within whirlpak bags. PAR was measured using an Walz US-SQS/L spherical quantum sensor with ULM-500 light meter. For Stas. 2 and 3, multiple PAR measurements were made at the surface, a few centimeters within the slurry and underneath larger ice sections with heavy snow. The irradiances were highly variable and thus we approximated the shading of around 50% of the surface. For Stas. 4–7, a hole was augured at 45° and PAR was measured every 5 cm through snow and ice until reaching seawater and then corrected for vertical depth.

All samples were stored in dark, insulated containers for a maximum of 4 h. Ice samples were melted in either a 3 : 1 or 1 : 1 volumetric ratio of melting solution to ice to minimize the effect of the melt on sea-ice communities (Campbell et al. 2019). The melting solution was 0.2-μm-filtered artificial salt mixture containing four main sea salts plus bicarbonate according to enriched seawater artifical water, artificial seawater (3.63×10^{-1} M NaCl, 4.71×10^{-2} M $MgCl_2{\cdot}6H_2O$, 2.5×10^{-2} M Na_2SO_4, 8.03×10^{-3} M KCl, and 2×10^{-3} M $NaHCO_3$, salinity 35; Harrison et al. 1980). Melts were conducted in the dark at approximately 20°C. To speed the melting process, ice samples were further broken into pieces with acid-washed pickaxes or acid-washed stainless steel meat forks. Most ice completely melted within 5 h. Volume and salinity were measured as soon as the ice was completely melted, with temperatures remaining below 3°C. Final salinities ranged from 27 to 32 for the 3 : 1 melts and 20 to 30 for the 1 : 1 melts (Supplementary Table S1). All reported volumes were corrected to the original ice volume.

POC, particulate nitrogen, and major nutrients

Samples for POC and particulate nitrogen were measured in 1 : 1 melts. Samples for major nutrients (NO_3^-, PO_4^{3-}, Si $[OH_4]$) were taken from direct melts (no addition of melting solution) of the physical cores. All samples were collected and processed according to protocols of the Marine Chemistry Laboratory at the University of Washington and UNESCO (1994; *see* Supplementary Text for more details). Unless otherwise stated, all values were reported as concentrations within bulk ice (ice plus brine).

Pigments

A subsample (50–250 mL) of 1 : 1 melt volume was gently filtered onto a 25-mm, 0.7-μm GF/F filter in the dark for pigment analysis by high-performance liquid chromatography (HPLC). Filters were flash-frozen in liquid nitrogen and stored at −80°C until analysis. Reverse-phase HPLC was conducted at the University of South Carolina after the method detailed by Pinckney et al. (1998). To estimate relative abundance of diatoms, *Phaeocystis*, and cryptophytes (as contribution to Chl *a* in μg L^{-1}), the respective diagnostic pigments of fucoxanthin, 19′ hexanoyloxyfucoxanthin, and alloxanthin were used as in Everitt et al. (1990) and Arrigo et al. (2000). Taxa abundances based on pigments were confirmed qualitatively via light microscopy.

Pigment concentrations by HPLC were used to calculate Chl *a*–specific absorption coefficient by microalgal pigments ($\overline{a}^*_{PHY}$), which could be further split into absorption coefficients for photosynthetic pigments ($\overline{a}^*_{PP}$) and photoprotective pigments ($\overline{a}^*_{PPC}$) following the methods described in Schuback and Tortell (2019; *see* Supplementary Text for more details).

^{14}C incubations

Rates of primary production were measured using ^{14}C incubations (Knap et al. 1996) with short (2 h) and long (e.g., dawn to dusk) incubations to estimate gross bottle production (GBP) and net bottle production in the light (NBP_L), respectively (*see* full details in Supplementary Text). Bottles were incubated in deckboard aquarium tanks, which were cooled with flow-through surface seawater and shaded to our best ability to mimic under-ice light conditions. Shading ranged from 50% to 6.75% transmission of surface irradiance with neutral density screens. For interior and bottom-ice stations, incubations received higher levels of irradiance than in situ (Supplementary Table S1). PAR during the incubations was logged by the ship mast PAR 2pi sensor (QSR-2100) and measured using our ULM 4-pi light meter inside the incubators to verify shading. Temperature within the tanks ranged between −1.8°C and −1.1°C for all incubations, which was close to the in situ temperatures (−2.2 to −1.8°C). Temperature was measured using a flow-through temperature sensor (HOBO) and confirmed with the thermometer used in our physical ice-core measurements.

Northern station (Stas. 1–4) samples were incubated approximately 18 h; southern station (Stas. 5–7) incubations were left for 24 h. Rates were normalized to Chl *a* and sea-ice volume. Temperature was measured using a flow-through temperature sensor (HOBO) and confirmed with the thermometer used in our physical ice-core measurements.

For comparison with our 2018 Rubisco-derived potential rates, we also included 2018 publicly available surface (~ 1 m) seawater measurements of ^{14}C fixation over 24 h taken by the Palmer-LTER team from their sampling Sta. B (Palmer Station Antarctica LTER and Waite 2022), the same location and time that our 2018 surface water samples were collected. Briefly, their bottle incubations are conducted in flow-through tanks without shading for 24 h using the above-described ^{14}C methods. As these incubations included 20 h of light plus 4 h of dark, we have denoted these measurements as net bottle production (NBP).

Active chlorophyll fluorescence

Fluorescence measurements were performed using a FIRe instrument (formerly SAtlantic, now Seabird). Samples of 15 mL were placed under low light (5 μmol photons m^{-2} s^{-1}) for 30 min at 3°C before measuring. Active fluorescent measurements consisted of a single turnover protocol from blue-emitting diodes (450 nm with 30 nm half bandwidth) with a saturation sequence of 120 μs flashlet and a relaxation

sequence of 60 pulses with 60 μs as the initial interval between relaxation pulses. A sequence interval of 1 s was repeated 10 times resulting in a total acquisition time of 10 s. Rapid fluorescent light curves (FLCs) were determined by sample measurements at 20 actinic irradiances from 0 to 200 μmol photons m^{-2} s^{-1}.

Parameters of photophysiology, including maximum quantum yield of photochemistry in Photosystem II (PSII) (F_v/F_m) and functional absorption cross section of PSII (σ_{PSII}), were calculated from the FIRe output after fitting the dark-acclimated data using phytoplankton photophysiology utilities (Ryan-Keogh and Robinson 2021) with blank and spectral corrections (*see* below for methods). The first flashlet was excluded, and a fixed connectivity parameter (ρ) of 0.3 was used (Babin 2008). From FLCs, we calculated electron transport rate at the reaction center of PSII (ETR_{RCII}, mol e^- mol $RCII^{-1}$ s^{-1}), initial slope (α_{ETR}), maximum ETR_{RCII}, and the light-saturation parameter (E_{k_RCII}, μmol photons m^{-2} s^{-1}; *see* full details in Supplementary Text).

Comparing ETR with ^{14}C fixation

The electron requirement for carbon fixation ($\phi_{e,C}$, mol e^- mol C^{-1}) is the ratio of ETR_{RCII} to CO_2 fixed. In a perfectly balanced system, four electrons are required to fix one CO_2 molecule. FIRe-derived rapid FLCs were used to calculate ETR_{RCII} for every minute during the 2 h midday ^{14}C incubation period using irradiances recorded by shipmast PAR sensors adjusted for shading. Total ETR_{RCII} was compared to total ^{14}C fixed over the same period. To enable direct comparisons of FIRe data with ^{14}C deckboard incubations, we first corrected for the different light spectra in the FIRe and in situ, and then converted the number of electrons per RCII to chlorophyll, using the approach of Schuback and Tortell (2019; *see* Supplementary Text for details).

Rubisco-derived, potential carbon fixation rates

Measured ^{14}C fixation rates were compared to potential carbon fixation rates calculated from Rubisco concentrations and an assumed Rubisco carboxylation rate (k^c_{cat}; Young et al. 2015; Roberts et al. 2024). To quantify Rubisco concentrations, subsamples (~0.5 liter) of 1 : 1 melt volume were filtered onto 0.2-μm Sterivex™ filters for proteomic analysis, except for samples from Sta. 3 which were collected onto 0.2-μm Nuclepore filters from a much lower sample volume (0.05 liter). Filters were promptly flash-frozen in liquid nitrogen and stored at −80°C pending analysis. Protein extraction and preparation for mass spectrometry was performed as in Wu et al. (2019). Measurements for the peptide of the large subunit of Rubisco (RbcL) were made via liquid chromatography–mass spectrometry using a Dionex Ultimate 3000 UPLC system interfaced with a TSQ Quantiva mass spectrometer run in selected reaction monitoring mode, as described (for different peptides) in Roberts et al. (2024; *see* Supplementary Text for more details).

Concentrations of RbcL (fmol L^{-1}) were converted to Rubisco content by normalizing to total protein (w/w; i.e., mg Rubisco mg TP^{-1}). Rubisco is a hexadecameric structure comprised of 8 RbcL and 8 small subunits (RbcS) with a molecular weight of Rubisco is 550 kDa (*see* Eq. 1).

$$[\text{Rubisco}] = [\text{RbcL}] \times \frac{1}{8} \times 550{,}000 \times \frac{10^{12}}{[\text{TP}]} \quad (1)$$

Concentrations of RbcL (fmol L^{-1}) were also converted to maximum potential carbon fixation rates (μmol C L^{-1} h^{-1}). Two active sites are formed within each of the four RbcL dimers within the enzyme. Thus, 1 mol RbcL = 1 mol active site. We assumed that all sites were active (to estimate potential C fixation rates) and temperature dependent with a carboxylation rate (k^c_{cat}) of 0.5 mol C mol^{-1} RbcL s^{-1} at approximately 0°C (Young et al. 2015; Eq. 2). The conversion factor of 1.8×10^{-6} converted fmol to μmol, seconds to hours and incorporated k^c_{cat}. These rates were compared to ^{14}C measurements.

$$\text{Potential C fixation rate} = [\text{RbcL}] \times 1.8 \times 10^{-6} \quad (2)$$

Results

Description of stations

Salinities and temperatures in our ice samples ranged from 32 to 38, and −1.7°C to −2.2°C, respectively, with temperatures lower, brine salinity higher and brine volume smaller in the slightly colder samples from Stas. 5 to 7 compared to Stas. 2 to 4 (Table 1). Light varied considerably between stations, with light transmission ranging from 0.1% in bottom-ice communities (Sta. 6) to an estimated 50% in rotten/brash ice (Stas. 2 and 3; Table 1; Supplementary Table S1). Full ice-core profiles of temperature, salinity, light, and calculated brine volume for Stas. 5–7 are publicly available (Young 2023*a*).

Dissolved major nutrient concentrations were higher in the underlying seawater than in bulk sea ice (Supplementary Table S5). NO_3^- and $Si(OH)_4$ were up to an order of magnitude higher in the underlying seawater at the interior and rotten/brash ice stations. NO_3^- concentrations were >1 μM across all ratios and dissolved N : P ratios were always lower than Redfield (16 : 1), suggesting that PO_4^{3-} was in excess, with the exception of bottom ice at Sta. 6. $Si(OH)_4$ concentrations varied but remained higher than nitrate. Nutrient concentrations within the brines would be 3–5 times higher, based on brine fractions.

Algal biomass in sea ice

All six sea-ice stations had ice that was visibly colored with algae. Values for POC, Chl *a*, and contributions of diatoms and *Phaeocystis* are shown in Supplementary Table S5. The full set of concentrations of pigments measured is publicly available (Young 2023*b*). POC concentrations in rotten/brash ice (Stas. 2 and 3) were more than double those measured in

Table 1. Sea-ice sampling locations grouped by ice type.

Sta.	Ice type	Location	Date	Ice thickness (cm)	Snow depth (cm)	Temp* (°C)	Brine salinity*	Brine vol. fraction*	E‡ (μmol photon m^{-2} s^{-1})
6	Bottom	67.774°S, 67.281°W	24 Nov	80 ± 7	8	−2.1 ± 0.43	39.8 ± 8.1	0.17 ± 0.07	12.4
5	Bottom	67.570°S, 68.196°W	21 Nov	87 ± 3	31	−1.8 ± 0.19	34.2 ± 3.6	0.22 ± 0.06	2.4
7	Interior	66.523°S, 67.545°W	05 Dec	135 ± 49	25	−2.0 ± 0.06	36.6 ± 1.1	0.24 ± 0.10	13
4	Interior	65.255°S, 64.216°W	13 Nov	55	13	−1.7	31.8	0.41	16
3	Rotten/brash	64.858°S, 64.020°W	11 Nov	n/a	n/a	−1.7	31.8	0.33 ± 0.02	~ 400
2	Rotten/brash	64.805°S, 64.235°W	10 Nov	n/a	n/a	−1.7	31.8	0.34 ± 0.07	~ 300

Error shows standard deviation of the mean ($n = 2$). Station labels are shaded for bottom (dark), interior (light), and rotten/brash (no shading).
*In situ measurements for samples collected in this study.
‡E at time of sampling.

bottom ice (Stas. 5 and 6). However, the opposite trend was found for Chl *a*, with concentrations in bottom ice more than double those measured in rotten/brash ice. At all stations, POC and Chl *a* were significantly higher in sea ice than in the underlying seawater. C : N ratios ranged from 7 to 9 within sea ice but were ~ 3 within the underlying seawater. Bottom ice (Stas. 5 and 6) had C : N values closer to Redfield than the other ice samples.

Diatoms were the dominant taxa at all stations, comprising 40–50% of Chl *a* biomass and up to 65% at Sta. 7. The next dominant taxa according to pigment abundance were haptophytes, which consisted primarily of colonial *Phaeocystis* (as determined by microscopy) and ranged from 0.5% to 40%

Fig. 2. Primary production (PP) by sea-ice algae, measured as NBP_L and GBP. (**a**) NBP_L (dark blue) and GBP (light blue), mean with standard deviation, normalized to area ($n = 2$ or 3) for each station (*see* Supplementary Table S6). Production per area was calculated from volume measurements, assuming production occurred in the visible algal bands which were 5–10 cm thick (average of 7.5 cm), with little production in underlying water. The same depth was applied to Stas. 2 and 3. Station labels are shaded for bottom (dark), interior (light), and rotten/brash (no shading). (**b**) NBP_L and GBP normalized to Chl *a* for each replicate (circles, color-coded by station). Solid line represents NBP_L = GBP; dashed lined, $NBP_L = 0.5 * GBP$.

of the Chl *a* biomass, equaling diatom abundance only at Sta. 4.

NBP_L and GBP production in sea ice

Sea-ice volume-normalized NBP_L rates ranged from approximately 2 to 49 mg C m^{-2} d^{-1} (Fig. 2a) or 3 to 42 mg C mg Chl a^{-1} d^{-1} (Fig. 2b; Supplementary Table S6). There was a high degree of variability between replicates at each station likely due to the heterogeneous sea-ice environment. NBP_L constituted a high proportion of GBP, with most ratios falling between 0.5 and 1.0 (Fig. 2b). There was no consistent difference in NBP_L : GBP between 18 h (Stas. 2–4) and 24 h (Stas. 5–7) incubations. For example, the two interior ice stations, Stas. 4 and 7, had the lowest and highest NBP_L : GBP, respectively. Bottom and interior ice stations, Stas. 4–7, received higher light intensities in the incubation than in situ (Supplementary Table S1) and thus the measured rates may not accurately represent rates in situ. No significant correlation was found between Chl *a* concentration and primary production rates (Supplementary Fig. S2).

Photophysiology

Dark-acclimated photochemical efficiency (F_v/F_m) was low, ranging between 0.15 and 0.25. While F_v/F_m was statistically different between stations (one-way ANOVA, *F*-value 6.32, *p*-value 0.02), there was no trend with ice type (Supplementary Table S7). The dark-acclimated functional cross section of PSII (σ_{PSII}) remained relatively constant across all stations with values of 1–1.5 nm^2, with no statistically significant differences between stations (Supplementary Table S7).

Rapid FLCs from 0 to 400 μmol photons m^{-2} s^{-1} highlighted differences in algal photophysiology across ice types (Fig. 3a–c; Supplementary Fig. S3 for curve fits; Supplementary Table S7). The light saturation parameter (E_{k_RCII}) varied between stations (one-way ANOVA, *F*-value 4.58, *p*-value < 0.046), with bottom-ice stations becoming saturated at low-light intensities (55 and 15 μmol photons m^{-2} s^{-1} for Stas. 5 and 6, respectively). Interior and rotten/brash-ice stations were saturated at much higher light intensities (E_{k_RCII} of 150–270 μmol photons m^{-2} s^{-1}). The initial slope of the FLC (α_{ETR}) ranged between 0.3 and 0.8 but with a high degree of variability, particularly within the bottom-ice stations (Stas. 5 and 6).

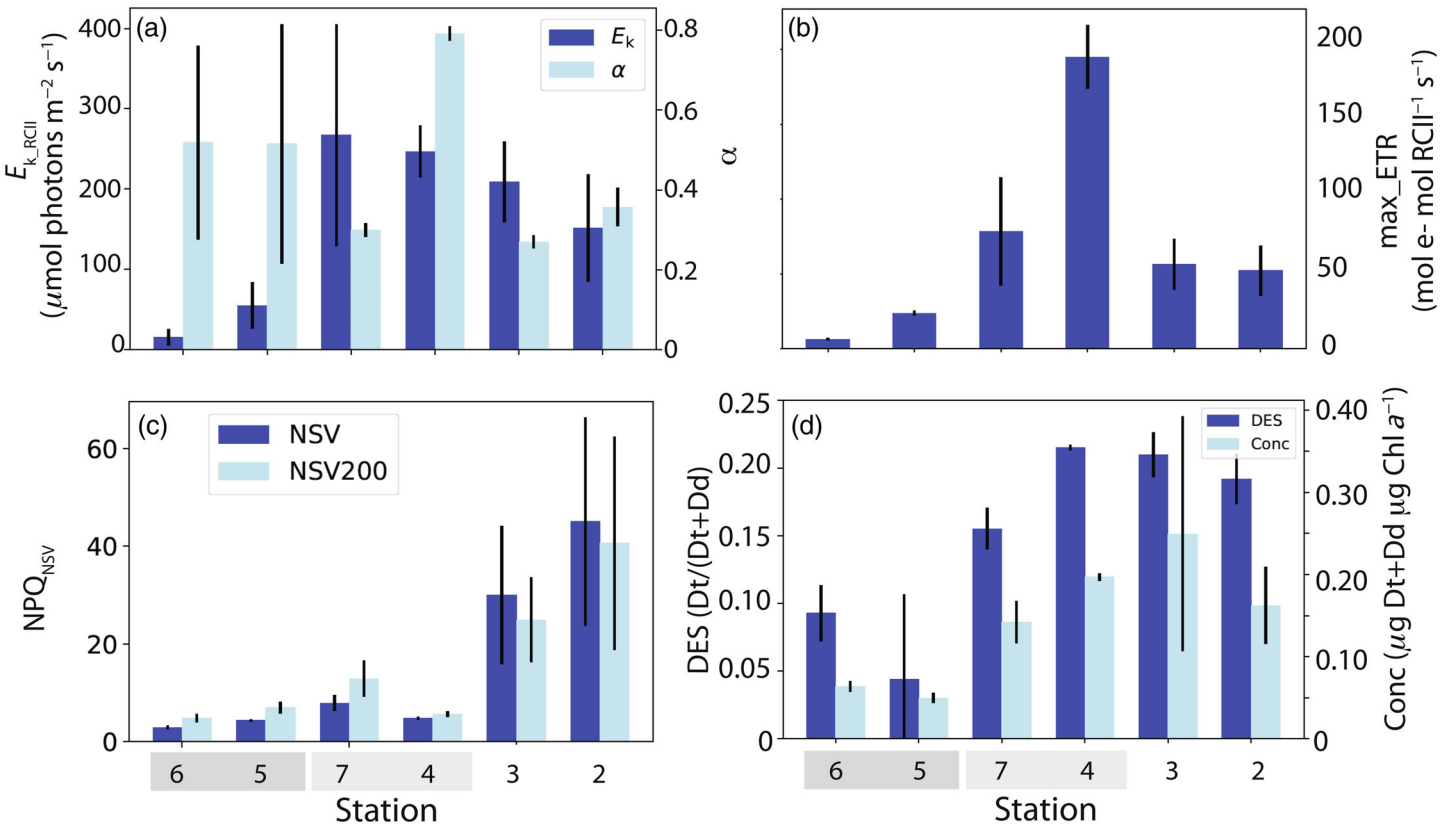

Fig. 3. Photophysiology from FLCs. (**a**) Light-saturation parameter (E_{k_RCII}, μmol photons m^{-2} s^{-1}; dark blue) and initial slope (α; light blue); (**b**) maximum rate of electron transport (max_ETR_{RCII}, mol e^- mol $RCII^{-1}$ s^{-1}); (**c**) non-photosynthetic quenching (normalized Stern–Volmer quenching, NPQ_{NSV}) during spectrally corrected, averaged midday irradiances in situ (dark blue) and at 200 μmol photons m^{-2} s^{-1} (light blue); and (**d**) de-epoxidation state (DES, w/w, dark blue) and Chl *a*-normalized concentrations (Conc, μg Chl a^{-1}, light blue) of the xanthophyll pigments, Dd and Dt, based on HPLC pigment analysis. Error bars show standard deviation of mean with $n = 2$–4 (*see* Supplementary Table S7). Station labels are shaded for bottom (dark), interior (light), and rotten/brash (no shading) ice.

Maximum electron transport rates (max_ETR$_{RCII}$) differed significantly between stations (one-way ANOVA, *F*-value 23.1, *p*-value < 0.001). Bottom-ice stations had the lowest rates of max_ETR$_{RCII}$, whereas interior-ice stations (particularly Sta. 4) had the highest max_ETR$_{RCII}$.

Non-photochemical quenching (NPQ$_{NSV}$), calculated for the average midday irradiance during ^{14}C incubations, varied significantly between stations (one-way ANOVA, *F*-value 5.63, *p*-value 0.029). Rotten/brash-ice stations had higher NPQ$_{NSV}$ compared to the other stations (Fig. 3c). To partially account for differences in irradiance between stations, NPQ$_{NSV}$ was also calculated at an arbitrary irradiance level of 200 μmol photons m^{-2} s^{-1}. The pattern of NPQ$_{NSV200}$ remained similar to NPQ$_{NSV}$ but significance was lost. Abundances and de-epoxidation states of xanthophyll cycle pigments, diadinoxanthin (Dd) and diatoxanthin (Dt) (Fig. 3d), varied significantly between stations (one-way ANOVA, *F*-value 5.2, *p*-value 0.017; *F*-value 11.7, *p*-value 0.001, respectively). Rotten/brash-ice stations had higher abundances and de-epoxidation states compared to bottom-ice stations. Interior-ice stations had abundances and de-epoxidation states of xanthophyll cycle pigments similar to the rotten/brash-ice stations.

The electron requirement for carbon fixation

The electron requirement for carbon fixation within the incubations ($\phi_{e,C}$, mol e$^-$ mol C^{-1}) was calculated by comparing estimated ETR$_{RCII}$ with the amount of carbon fixed at midday (Chl *a*-normalized GBP; *see* Methods). Values of $\phi_{e,C}$ were highest at Stas. 2 and 3 with values of 13 ± 4 and 19 ± 10 ($n = 2$), respectively (Table 2). In contrast, Stas. 4–6 all had values closer to 4 mol e$^-$ mol C^{-1}, whereas Sta. 7 was roughly double that value (7 ± 1 mol e$^-$ mol C^{-1}).

Potential carbon fixation rates based on Rubisco content

Rubisco content (normalized to total protein, w/w) in our sea-ice samples and surface seawater (collected in 2018) are shown in Fig. 4a. The range of Rubisco content in the sea-ice samples varied significantly from 2% to 5% (w/w) of total protein across all stations (one-way ANOVA, *F*-statistic 23.2, *p*-value < 10^{-6}), with interior-ice algae at Sta. 4 having the lowest concentrations and bottom-ice algae having the highest content. Rubisco content from underlying seawater was not measured but surface seawater samples from 2018 had Rubisco content around 6–8%.

Rubisco concentrations were converted to potential carboxylation rates (assuming a k^c_{cat} of 0.5 C s^{-1}; *see* Methods) and compared to NBP$_L$ from sea ice (Fig. 4b) and the NBP from surface seawater in 2018. Potential carbon fixation rates estimated from Rubisco concentrations displayed close agreement with measured NBP from seawater and NBP$_L$ from interior sea-ice (Stas. 4 and 7) and one rotten/brash ice stations (Sta. 2). In contrast, bottom-ice algae (Stas. 5 and 6) had approximately fivefold higher Rubisco-derived carbon fixation rates than the measured NBP$_L$ or GBP (Fig. 4b). Sta. 3 was unusual as potential carbon fixation rates from Rubisco concentrations were 10-fold higher than NBP$_L$.

Discussion

The contribution of sea-ice algae to coastal marine primary production

Our rates add to the few published measurements of sea-ice algal primary production along the western Antarctic Peninsula (Selz et al. 2018; van Leeuwe et al. 2022). The NBP$_L$ rates of 2–49 mg C m^{-2} d^{-1} are comparable to other Antarctic sea-ice measurements (Table 3, updated from Arrigo 2017). Our measurements likely underestimated sea-ice primary production, as we only accounted for production within the 5–10 cm of ice where a visible algal band was present, yet primary production likely extended farther through the core. Additionally, our measurements approximate potential rates rather than true in situ rates due to higher light intensities during incubations at Stas. 4–7 (> 100 μmol photon m^{-2} s^{-1} for Stas. 4–6) and the addition of dissolved inorganic carbon (2 mM). The ice environment sampled likely had a high degree of exchange with seawater and we thus assumed our artificial addition of HCO_3^- to be reasonable for rate measurements. Although conditions within brines can be dynamic, studies have shown that sea-ice algae

Table 2. Parameters to calculate the electron requirement for carbon fixation ($\phi_{e,C}$, mol e$^-$ mol C^{-1}).

Sta.	Sample type	*n*	1/nPSII (mol Chl *a* mol RCII^{-1})	$\overline{a}^*_{PHY}$ (mg Chl *a*$^{-1}$)	Midday ETR (mol e$^-$ mol Chl *a*$^{-1}$ 2 h^{-1})	$\phi_{e,C}$ (mol e$^-$: mol C)
6	Bottom	2	323 ± 34	0.007 ± 0.00	142 ± 17	5 ± 1
5	Bottom	2	375 ± 27	0.005 ± 0.00	381 ± 101	3 ± 1
7	Interior	2	232 ± 37	0.005 ± 0.00	784 ± 135	7 ± 1
4	Interior	2	223 ± 6	0.007 ± 0.00	1889 ± 52	4 ± 1
3	Rotten/brash	2	269 ± 37	0.007 ± 0.00	1464 ± 448	19 ± 10
2	Rotten/brash	2	264 ± 9	0.006 ± 0.00	1356 ± 366	13 ± 4

n denotes number of replicates. Error denotes standard deviation of the mean. Station labels are shaded for bottom (dark), interior (light), and rotten/brash (no shading).

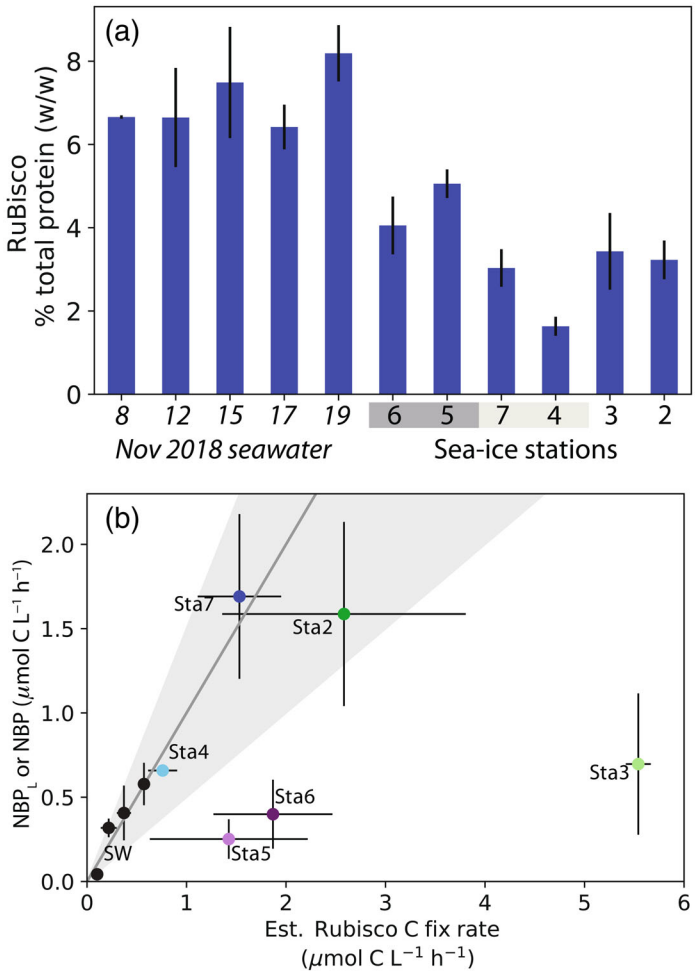

Fig. 4. (**a**) Rubisco content: total protein (%w/w) for 2018 seawater and 2019 sea-ice samples. *X*-axis labels identify dates of sampling for seawater (left) and station number for sea-ice samples (right). Station labels are shaded for bottom (dark), interior (light), and rotten/brash (no shading) ice. (**b**) NBP_L (sea ice) and NBP (seawater) vs. potential carbon fixation rates based on Rubisco concentrations. Solid line represents 1 : 1 line ± 50% shown by shading. Error bars are standard deviation of mean ($n = 2$). Color coding is the same as Fig. 2b.

are largely insensitive to ocean acidification (Hoppe et al. 2018) and have little effect on the carbonate chemistry of underlying seawater during spring (Else et al. 2019).

At the time of sampling there was little phytoplankton biomass in the underlying water column. However, under-ice phytoplankton blooms have been observed along the western Antarctic Peninsula in other years (e.g., Arrigo et al. 2017). The timing of sea-ice algal blooms and their potential carbon export (Koch et al. 2023) could play an important quantitative role in coastal marine ecosystems along the western Antarctic Peninsula. The magnitude of sea-ice algal production measured here (2–49 mg C m^{-2} d^{-1}) is comparable to rates measured for surface phytoplankton in this region, though at the lower end of the range when compared to depth-integrated pelagic primary production. For comparison, the 30-yr record of depth-integrated NBP near Palmer Station (Sta. B, PAL-LTER sampling grid), which is often ice free in November, ranges from 40 to 8 g C m^{-2} d^{-1} (Schofield et al. 2018; Palmer Station Antarctica LTER and Waite 2022).

The high ratios of NBP_L : GBP (~ 0.5–1.0) were similar to ratios of 0.6–0.9 observed during a coastal seawater spring bloom of diatoms in the western Antarctic Peninsula (Goldman et al. 2015) and in cultured polar phytoplankton (Lacour et al. 2022). High ratios suggest high assimilation efficiency of fixed carbon in polar waters. The rates are given in mg C mg Chl a^{-1} d^{-1} but only pertain to the 2-h period of incubation and so these ratios could vary over the course of the day.

Factors controlling photosynthesis during the spring melt of sea ice

Our approach combined multiple methods that measured different components of photosynthesis, each with caveats, different timescales and experimental conditions. Despite these caveats, there were consistencies between methods giving confidence to cross-comparisons: FLC-derived parameters of max_ETR_{RCII} correlated positively with incubation-derived rates of chlorophyll-normalized NBP_L and GBP; FLC-derived calculation of NPQ_{NSV} agreed well with xanthophyll pigments for rotten/brash-ice and bottom-ice stations; and potential carboxylation rates based on Rubisco concentrations were never below measured rates of GBP.

We found that the physical environment was an important factor in determining photosynthesis in our samples, as trends in photophysiology and productivity related largely to ice type (bottom, interior, rotten/brash). All samples were otherwise similar in being diatom-dominated (approximately 50%), coastal, and macronutrient-replete. It is possible that our algal communities were Fe-limited, as suggested by high C : N and C : Chl *a* ratios and low F_v/F_m values across all our samples (Supplementary Tables S5, S6). Fe limitation in the Southern Ocean is known to have a significant impact on phytoplankton physiology (Schallenberg et al. 2020). However, Joy-Warren et al. (2022) found that Fe did not limit spring phytoplankton growth despite low concentrations in this region. In Fig. 5, we provide a conceptual visualization summarizing the different photosynthetic strategies of algae observed across bottom, interior, and rotten/brash ice.

Bottom-ice algae

Less than 1% of surface light reached the algae in bottom ice (Supplementary Table S1). Bottom-ice algae have large antennae (as indicated by large $1/n_{PSII}$, Table 2) to optimize light harvesting but electron transport around PSII was likely light-limited as E_{k_RCII} was below in situ light levels (< 50 μmol photons m^{-2} s^{-1} compared to < 15 μmol photons m^{-2} s^{-1}, respectively), with values similar to other bottom-ice samples (van Leeuwe et al. 2022). The bottom-ice stations also had

Table 3. Net production measurements from Antarctic sea ice, including this study along the western Antarctic Peninsula (table updated from Arrigo 2017).

Ice type	Region	Season	Daily (mg C m^{-2} d^{-1})	References
Bottom	McMurdo Sound	Spring	0.5–85	(Grossi et al. 1987)
Bottom	Prydz Bay	Spring	4.6	(Archer et al. 1996)
Bottom (fast)	Western Antarctic Peninsula (**Stas. 5 and 6**)	**Spring**	**4–15**	**This study***
Bottom	Casey Station	Spring	103	(McMinn et al. 2012)
Platelet	McMurdo Sound	Spring	2–1250	(Grossi et al. 1987)
Platelet	McMurdo Sound	Spring	200–1200	(Arrigo et al. 1995)
Interior	McMurdo Sound	Summer	0.5–12	(Stoecker et al. 2000)
Interior (pack)	Western Antarctic peninsula (**Stas. 4 and 7**)	**Spring**	**9–49**	**This study***
New	Weddell Sea	Autumn	0.02–0.25	(Mock 2002)
Pack	Bransfield Straight	Winter	42–60	(Kottmeier et al. 1987)
Rotten/brash	Western Antarctic peninsula (**Stas. 2 and 3**)	**Spring**	**2–49**	**This study***

*Range accounting for each individual sample measured in our study.

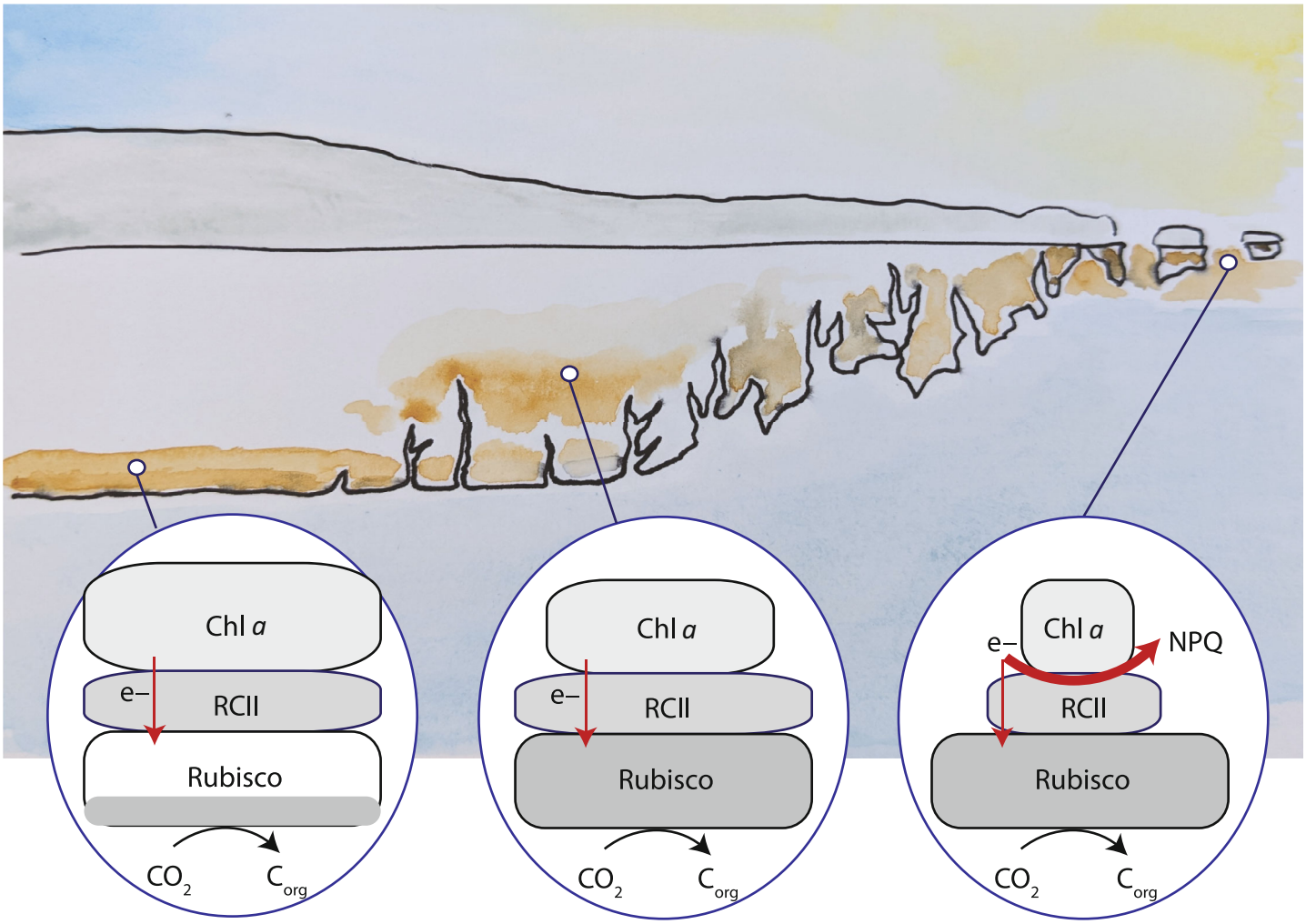

Fig. 5. Conceptual visualization of photosynthesis strategies, converting CO_2 to organic carbon (C_{org}), for different sea-ice environments during spring melt. Left: bottom sea-ice algae (e.g., Stas. 5 and 6) have large pools of Chl *a* and PSII reaction centers (RCII) to capture low light; Rubisco is highly abundant but not operating at full capacity. Middle: interior sea-ice algae (e.g., Stas. 4 and 7) have increased RCII pools to adapt to higher light levels; Rubisco is fully active. Right: rotten/brash-ice algae (e.g., Stas. 2 and 3) have reduced Chl *a* and RCII pools and increased NPQ to adapt to high light; Rubisco is fully active.

lower max_ETR_{RCII} and Chl *a*-normalized GBP compared to other stations, which may have been a result of pigment packaging due to low-light conditions (Ferreira et al. 2017). It is possible that the warmer temperature (3°C) during FLC measurements could have increased saturation of PSII (Balfagón et al. 2022), which could explain the low F_v/F_m values but not the low NPQ_{NSV} that was observed in our interior and bottom-ice samples.

The ratio $\phi_{e,C}$ based on incubations was approximately 4, indicating that most electrons were being utilized for carbon fixation. As this ratio depends on comparing different methods (FLC vs. ^{14}C incubations), $\phi_{e,C}$ should be considered as approximate. In situ, lower light levels would make it unlikely that $\phi_{e,C}$ could be higher (Supplementary Fig. S4). In contrast, potential rates of carbon fixation based on Rubisco exceeded NBP_L and GBP. As samples for Rubisco were frozen immediately on melting, we presumed they are representative of in situ concentrations. Thus, either bottom-ice algae maintain excess Rubisco in situ in preparation for increasing light levels (as has been observed during the onset of winter; Lacour et al. 2019), or photoinhibition occurred within the incubations. We surmised that photoinhibition was unlikely as FLC-derived NPQ_{NSV} and ETR_{RCII} calculated for the light intensities at midday during the incubations were low, though comparisons of different methods need to be treated with caution. Overall, our results indicated that the light reaction, not the rate of Rubisco carboxylation, was limiting primary production in bottom-ice algae.

Interior-ice algae

As sea ice begins to melt, rafted floes can create flooded interior layers. Both Stas. 4 and 7 had middle layers with large gaps, dense algal growth, and even juvenile krill, though ice thickness at Stas. 7 was more than double that of Sta. 4. Sta. 4 had the highest max_ETR_{RCII} correlating with the highest rates of GBP. Sta. 4 also had a high concentration of colonial *Phaeocystis* (40% of the algal composition), perhaps making this response taxon-specific (Supplementary Table S5). Colonial *Phaeocystis* exude high amounts of dissolved organic carbon, which may account for the lower ratio of NBP_L : GBP at Sta. 4.

Interior algae at Stas. 4 and 7 received slightly higher light intensities in situ but also had approximately fourfold higher E_{k_RCII} than bottom-ice algae. Maximum light intensities received during the incubations also remained below the E_{k_RCII} (Supplementary Fig. S4), suggesting that their PSII was also light-limited. Low values for NPQ_{NSV} and a relatively low $\phi_{e,C}$ (4 and 7, mol e^- mol C^{-1} for Stas. 4 and 7, respectively) both suggest that the majority of ETR_{RCII} was channeled toward carbon fixation. However, HPLC-derived pigment data showed abundances and de-epoxidation states of xanthophyll cycle pigments that closely matched the rotten/brash-ice stations and indicated acclimation for high-light conditions in situ. Differences between NPQ_{NSV} and pigment data may have arisen during sample collection or conditions during FLC curves, or signal a real physiological difference. Potential rates of carbon fixation based on Rubisco closely matched NBP_L; thus even under saturating light intensities, carbon fixation rates could not increase unless Rubisco concentrations were also increased.

Rotten/brash-ice algae

Algae at Stas. 2 and 3 were inhabiting ice that was heavily disintegrated in structure due to advanced melt and water movement. Incident irradiation at midday of ~ 600–800 μmol photons m^{-2} s^{-1} (Supplementary Fig. S4) greatly exceeded an E_{k_RCII} of 150–200 μmol photons m^{-2} s^{-1} (Fig. 3a) and also likely saturated CO_2 fixation, which could be saturated at much higher light levels than E_{k_RCII} (Schuback et al. 2015). Rotten/brash-ice stations had higher NPQ_{NSV} compared to other stations (Fig. 3c) and high abundances and de-epoxidation state of the xanthophyll cycle pigments, Dd and Dt, an indication of responding to high light conditions (Fig. 3d). The ratio $\phi_{e,C}$ was > 10, indicating that most electrons were not directed to carbon fixation and instead dissipated through either NPQ or fluorescence. Potential carbon fixation rates based on Rubisco matched measured NBP_L for Sta. 2 and NBP for our surface seawater phytoplankton. However, Sta. 3 had 10-fold higher potential carbon fixation rates than NBP_L. High NBP_L : GBP indicated that difference could not be due to respiration lowering NBP_L. Instead, it was likely an artifact due to anonymously high total protein concentrations at Sta. 3 (0.7 μg protein μg POC^{-1}) compared to other stations (Supplementary Tables S5, S8) which also did not agree with high C : N ratios at Sta. 3 of > 8. Protein samples for Sta. 3 were collected on a different filter (0.2 μm Nuclepore instead of 0.2 μm sterivex) from a much lower sample volume (0.05 liter vs. ~ 0.5 liter). We suspect that in our rotten/brash ice stations and surface seawater samples, light was saturating PSII both in situ and in the incubations, driving an excess in ETR_{RCII} needed for carbon fixation. Instead, carbon fixation rates were related to Rubisco concentrations.

Approaches to measuring primary production in sea ice

Measuring primary production in sea ice is challenging. There is a need for new approaches. Absorption spectra have already been shown to be a better predictor of Southern Ocean phytoplankton primary production than chlorophyll alone (Kerkar et al. 2021). Previous studies have also proposed the use of active fluorescence to estimate carbon fixation rates (Zhu et al. 2017), though most phytoplankton studies to date have found $\phi_{e,C}$ to be much higher than 4 and to correlate with NPQ rather than primary production (Schuback et al. 2015; Schuback and Tortell 2019). Selz et al. (2018) found that prior light history was a major driver of photophysiology of *Phaeocystis*-dominated communities associated in slush layers along the western Antarctic Peninsula. While they did not measure $\phi_{e,C}$, they reported maximum carbon

fixation rates similar in magnitude to our interior and rotten/brash ice samples while E_{k_RCII} and F_v/F_m were similar to our bottom-ice samples. While our data hint that bottom and interior sea ice may provide environmental conditions suitable for using $\phi_{e,C}$ to estimate GBP, more work is needed to understand the environmental mechanisms driving $\phi_{e,C}$ in ice algal communities.

Rubisco concentrations provided a reasonable estimate of measured NBP_L in surface seawater, a sample of rotten/brash ice and interior layers of sea ice, but overestimated rates for bottom-ice algae. Previous studies have suggested that Rubisco concentrations could be used to estimate potential maximum carbon fixation rates in phytoplankton (Losh et al. 2013; Young et al. 2015; Roberts et al. 2024). This approach would require that all Rubisco be fully active and not substrate-limited and that accurate estimates of its carboxylation rate be available. To reflect actual carbon fixation rates, cellular Rubisco content would also need to be regulated with growth rate. We suggest that there is evidence that these requirements are often met in polar oceans. Losh et al. (2013) and Young et al. (2015) found Rubisco to be fully active and CO_2-saturated in phytoplankton. While carboxylation rates of Rubisco vary between taxa, diatoms and haptophytes have similar Rubisco carboxylation rates (Young et al. 2016) and any differences are reduced at cold temperatures (Galmés et al. 2016; Roberts et al. 2024). There is still debate on whether cellular Rubisco content is regulated with growth rate. Neither light nor temperature affect Rubisco content in diatoms (Mock and Hoch 2005; Lacour et al. 2019); however, Rubisco content is reduced during stationary phase and under N and/or P limitation (Losh et al. 2013). Although nitrogen concentrations are high in the Southern Ocean, energy for intracellular nitrogen cycling requires photosynthetically derived NADP and ATP, such that Fe or other trace metal limitations could indirectly impact energy-intensive cellular processes (Schoffman et al. 2016).

Although more work is needed, we suggest that Rubisco concentrations could be used to calculate NBP_L in polar oceans when light is saturating, such as in surface seawater and possibly sea ice in an advanced stage of melt. In addition, mass spectrometry-based proteomics, which enables quantification of RbcL peptides belonging to different photosynthetic groups, could lead to taxon-specific measurements of primary production in polar oceans (Roberts et al. 2024).

Conclusions

This work quantified primary production by sea-ice algae within coastal waters near the western Antarctic Peninsula in Spring 2019 and demonstrated the importance of sea-ice algal productivity to total primary production within this region, especially when under-ice phytoplankton productivity is low. The physiological strategies that underpin rates of carbon fixation in sea-ice were uncovered, including how sea-ice algae acclimate photophysiology to highly variable light levels during Spring melt but other factors, such as Rubisco concentrations, are also important to consider.

Data availability statement

Source data are provided with this paper and deposited at the US Antarctic Program Data Center (USAP-DC) under award number 1744645.

References

Archer, S., R. Leakey, P. Burkill, M. Sleigh, and J. Appleby. 1996. Microbial ecology of sea ice at a coastal Antarctic site: Community composition, biomass and temporal change. Mar. Ecol. Prog. Ser. **135**: 179–195. doi:10.3354/meps135179

Arrigo, K. R. 2017. Sea ice as a habitat for primary producers, p. 352–369. *In* D. N. Thomas [ed.], Sea ice. John Wiley & Sons, Ltd. doi:10.1002/9781118778371.ch14

Arrigo, K. R., G. Dieckmann, M. Gosselin, D. H. Robinson, C. H. Fritsen, and C. W. Sullivan. 1995. High resolution study of the platelet ice ecosystem in McMurdo Sound, Antarctica biomass, nutrient, and production profiles within a dense microalgal bloom. Mar. Ecol. Prog. Ser. **127**: 255–268. doi:10.3354/meps127255

Arrigo, K. R., G. R. DiTullio, R. B. Dunbar, D. H. Robinson, M. VanWoert, D. L. Worthen, and M. P. Lizotte. 2000. Phytoplankton taxonomic variability in nutrient utilization and primary production in the Ross Sea. J. Geophys. Res. Oceans **105**: 8827–8846. doi:10.1029/1998jc000289

Arrigo, K. R., and others. 2017. Early spring phytoplankton dynamics in the western Antarctic Peninsula. J. Geophys. Res. Oceans **122**: 9350–9369. doi:10.1002/2017JC013281

Babin, M. 2008. Phytoplankton fluorescence: Theory, current literature and in situ measurement, p. 237–280. *In* M. Babin, C. Roesler, and J. Cullen [eds.], Real-time coastal observing systems for marine ecosystem dynamics and harmful algal blooms. Scientific and Cultural Organization.

Balfagón, D., S. I. Zandalinas, T. D. R. de Oliveira, C. Santa-Catarina, and A. Gómez-Cadenas. 2022. Reduction of heat stress pressure and activation of photosystem II repairing system are crucial for citrus tolerance to multiple abiotic stress combination. Physiol. Plant. **174**: e13809. doi:10.1111/ppl.13809

Bernard, K. S., and others. 2019. The contribution of ice algae to the winter energy budget of juvenile Antarctic krill in years with contrasting sea ice conditions. ICES J. Mar. Sci. **76**: 206–216. doi:10.1093/icesjms/fsy145

Bozzato, D., T. Jakob, and C. Wilhelm. 2019. Effects of temperature and salinity on respiratory losses and the ratio of photosynthesis to respiration in representative Antarctic phytoplankton species. PLoS One **14**: e0224101. doi:10.1371/journal.pone.0224101

Campbell, K., and others. 2019. Melt procedure affects the photosynthetic response of sea ice algae. Front. Earth Sci. **7**: 21.

Cox, G. F. N., and W. F. Weeks. 1986. Changes in the salinity and porosity of sea-ice samples during shipping and storage. J. Glaciol. **32**: 371–375. doi:10.3189/S0022143000012065

Dawson, H. M., and others. 2023. Microbial metabolomic responses to changes in temperature and salinity along the western Antarctic Peninsula. ISME J. **17**: 2035–2046. doi:10.1038/s41396-023-01475-0

Else, B. G., J. J. Whitehead, V. Galindo, J. Ferland, C. J. Mundy, S. F. Gonski, J. K. Ehn, S. Rysgaard, and M. Babin. 2019. Response of the Arctic marine inorganic carbon system to ice algae and under-ice phytoplankton blooms: A case study along the fast-ice edge of Baffin Bay. J. Geophys. Res. Oceans **124**: 1277–1293. doi:10.1029/2018JC013899

Everitt, D. A., S. W. Wright, J. K. Volkman, D. P. Thomas, and E. J. Lindstrom. 1990. Phytoplankton community compositions in the western equatorial Pacific determined from chlorophyll and carotenoid pigment distributions. Deep Sea Res. A Oceanogr. Res. Pap. **37**: 975–997. doi:10.1016/0198-0149(90)90106-6

Ferreira, A., Á. M. Ciotti, C. R. B. Mendes, J. Uitz, and A. Bricaud. 2017. Phytoplankton light absorption and the package effect in relation to photosynthetic and photoprotective pigments in the northern tip of Antarctic Peninsula. J. Geophys. Res. Oceans **122**: 7344–7363. doi:10.1002/2017JC012964

Frankenstein, G., and R. Garner. 1967. Equations for determining the brine volume of sea ice from −0.5° to −22.9°C. J. Glaciol. **6**: 943–944. doi:10.3189/S0022143000020244

Galmés, J., C. Hermida-Carrera, L. Laanisto, and Ü. Niinemets. 2016. A compendium of temperature responses of Rubisco kinetic traits: Variability among and within photosynthetic groups and impacts on photosynthesis modeling. J. Exp. Bot. **67**: 5067–5091. doi:10.1093/jxb/erw267

Goldman, J. A. L., S. A. Kranz, J. N. Young, P. D. Tortell, R. H. R. Stanley, M. L. Bender, and F. M. M. Morel. 2015. Gross and net production during the spring bloom along the Western Antarctic Peninsula. New Phytol. **205**: 182–191. doi:10.1111/nph.13125

Grossi, S. M., S. T. Kottmeier, R. L. Moe, G. T. Taylor, and C. W. Sullivan. 1987. Sea ice microbial communities. VI. Growth and primary production in bottom ice under graded snow cover. Mar. Ecol. Prog. Ser. **35**: 153–164.

Harrison, P. J., R. E. Waters, and F. J. R. Taylor. 1980. A broad spectrum artificial seawater medium for coastal and open ocean phytoplankton. J. Phycol. **16**: 28–35. doi:10.1111/j.0022-3646.1980.00028.x

Hoppe, C. J. M. 2022. Always ready? Primary production of Arctic phytoplankton at the end of the polar night. Limnol. Oceanogr. Lett. **7**: 167–174. doi:10.1002/lol2.10222

Hoppe, C. J. M., and others. 2018. Compensation of ocean acidification effects in Arctic phytoplankton assemblages. Nat. Clim. Change **8**: 529–533. doi:10.1038/s41558-018-0142-9

Huner, N. P. A., G. Öquist, and F. Sarhan. 1998. Energy balance and acclimation to light and cold. Trends Plant Sci. **3**: 224–230. doi:10.1016/S1360-1385(98)01248-5

Jacquemot, L., A. Vigneron, J.-É. Tremblay, and C. Lovejoy. 2022. Contrasting sea ice conditions shape microbial food webs in Hudson Bay (Canadian Arctic). ISME Comm. **2**: 104. doi:10.1038/s43705-022-00192-7

Joy-Warren, H. L., and others. 2019. Light is the primary driver of early season phytoplankton production along the western Antarctic Peninsula. J. Geophys. Res. Oceans **124**: 7375–7399. doi:10.1029/2019JC015295

Joy-Warren, H. L., and others. 2022. Springtime phytoplankton responses to light and iron availability along the western Antarctic Peninsula. Limnol. Oceanogr. **67**: 800–815. doi:10.1002/lno.12035

Kattner, G., D. N. Thomas, C. Haas, and H. Kennedy. 2004. Surface ice and gap layers in Antarctic sea ice: Highly productive habitats. Mar. Ecol. Prog. Ser. **277**: 1–12.

Kerkar, A. U., S. C. Tripathy, D. J. Hughes, P. Sabu, S. R. Pandi, A. Sarkar, and M. Tiwari. 2021. Characterization of phytoplankton productivity and bio-optical variability in a polar marine ecosystem. Prog. Oceanogr. **195**: 102573. doi:10.1016/j.pocean.2021.102573

Knap, A. H., A. Michaels, A. R. Close, H. Ducklow, and A. G. Dickson. 1996. Protocols for the joint global ocean flux study (JGOFS) core measurements, p. 170. *In* JGOFS, Reprint of the IOC Manuals and Guides No. 29, UNESCO 1994, v. **19**. UNESCO. doi:10.25607/OBP-1409

Koch, C. W., and others. 2023. Year-round utilization of sea ice-associated carbon in Arctic ecosystems. Nat. Commun. **14**: 1964. doi:10.1038/s41467-023-37612-8

Kottmeier, S. T., S. M. Grossi, and C. W. Sullivan. 1987. Sea ice microbial communities. VIII. Bacterial production in annual sea ice of McMurdo Sound, Antarctica. Mar. Ecol. Prog. Ser. **35**: 175–186.

Kvernvik, A. C., S. D. Rokitta, E. Leu, L. Harms, T. M. Gabrielsen, B. Rost, and C. J. M. Hoppe. 2020. Higher sensitivity towards light stress and ocean acidification in an Arctic sea-ice-associated diatom compared to a pelagic diatom. New Phytol. **226**: 1708–1724. doi:10.1111/nph.16501

Kvernvik, A., C. Hoppe, M. Greenacre, S. Verbiest, J. Wiktor, T. Gabrielsen, M. Reigstad, and E. Leu. 2021. Arctic sea ice algae differ markedly from phytoplankton in their ecophysiological characteristics. Mar. Ecol. Prog. Ser. **666**: 31–55.

Lacour, T., J. Larivière, and M. Babin. 2017. Growth, Chl *a* content, photosynthesis, and elemental composition in polar and temperate microalgae. Limnol. Oceanogr. **62**: 43–58. doi:10.1002/lno.10369

Lacour, T., J. Larivière, J. Ferland, F. Bruyant, J. Lavaud, and M. Babin. 2018. The role of sustained photoprotective non-photochemical quenching in low temperature and high

light acclimation in the bloom-forming arctic diatom *Thalassiosira gravida*. Front. Mar. Sci. **5**. doi:10.3389/fmars.2018.00354

Lacour, T., P.-I. Morin, T. Sciandra, N. Donaher, D. A. Campbell, J. Ferland, and M. Babin. 2019. Decoupling light harvesting, electron transport and carbon fixation during prolonged darkness supports rapid recovery upon re-illumination in the Arctic diatom *Chaetoceros neogracilis*. Polar Biol. **42**: 1787–1799. doi:10.1007/s00300-019-02507-2

Lacour, T., and others. 2022. Photoacclimation of the polar diatom *Chaetoceros neogracilis* at low temperature. PLoS One **17**: e0272822.

Losh, J. L., J. N. Young, and F. M. M. Morel. 2013. Rubisco is a small fraction of total protein in marine phytoplankton. New Phytol. **198**: 52–58. doi:10.1111/nph.12143

Lund-Hansen, L. C., I. Hawes, K. Hancke, N. Salmansen, J. R. Nielsen, L. Balslev, and B. K. Sorrell. 2020. Effects of increased irradiance on biomass, photobiology, nutritional quality, and pigment composition of Arctic sea ice algae. Mar. Ecol. Prog. Ser. **648**: 95–110.

McMinn, A., C. Ashworth, R. Bhagooli, A. Martin, S. Salleh, P. Ralph, and K. Ryan. 2012. Antarctic coastal microalgal primary production and photosynthesis. Mar. Biol. **159**: 2827–2837. doi:10.1007/s00227-012-2044-0

Mock, T. 2002. In situ primary production in young Antarctic sea ice. Hydrobiologia **470**: 127–132. doi:10.1023/A:1015676022027

Mock, T., and N. Hoch. 2005. Long-term temperature acclimation of photosynthesis in steady-state cultures of the polar diatom *Fragilariopsis cylindrus*. Photosynth. Res. **85**: 307–317. doi:10.1007/s11120-005-5668-9

Palmer Station Antarctica LTER, and N. Waite. 2022. Merged discrete water-column data from annual PAL LTER field seasons at Palmer Station, Antarctica, from 1991 to 2021. Environmental Data Initiative. doi:10.6073/pasta/7358be99bd7ec1c73293893defb289d3

Pinckney, J. L., H. W. Paerl, M. B. Harrington, and K. E. Howe. 1998. Annual cycles of phytoplankton community-structure and bloom dynamics in the Neuse River Estuary, North Carolina. Mar. Biol. **131**: 371–381.

QGIS.org 2024. QGIS geographic information system. QGIS Association. http://www.qgis.org

Roberts, M. E., and others. 2024. Rubisco in high Arctic tidewater glacier-marine systems: A new window into phytoplankton dynamics. Limnol. Oceanogr. **69**: 802–817. doi:10.1002/lno.12525

Ryan-Keogh, T. J., and C. M. Robinson. 2021. Phytoplankton photophysiology utilities: A Python toolbox for the standardization of processing active chlorophyll-a fluorescence data. Front. Mar. Sci. **8**: 525414. doi:10.3389/fmars.2021.525414

Schallenberg, C., R. F. Strzepek, N. Schuback, L. A. Clementson, P. W. Boyd, and T. W. Trull. 2020. Diel quenching of Southern Ocean phytoplankton fluorescence is related to iron limitation. Biogeosciences **17**: 793–812. doi:10.5194/bg-17-793-2020

Schoffman, H., H. Lis, Y. Shaked, and N. Keren. 2016. Iron–nutrient interactions within phytoplankton. Front. Plant Sci. **7**: 1223. doi:10.3389/fpls.2016.01223

Schofield, O., M. Brown, J. Kohut, S. Nardelli, G. Saba, N. Waite, and H. Ducklow. 2018. Changes in the upper ocean mixed layer and phytoplankton productivity along the West Antarctic Peninsula. Philos. Trans. A Math. Phys. Eng. Sci. **376**: 20170173. doi:10.1098/rsta.2017.0173

Schuback, N., C. Schallenberg, C. Duckham, M. Maldonado, and P. Tortell. 2015. Interacting effects of light and iron availability on the coupling of photosynthetic electron transport and CO_2-assimilation in marine phytoplankton. PLoS One **10**: e0133235. doi:10.1371/journal.pone.0133235

Schuback, N., and P. D. Tortell. 2019. Diurnal regulation of photosynthetic light absorption, electron transport and carbon fixation in two contrasting oceanic environments. Biogeosciences **16**: 1381–1399. doi:10.5194/bg-16-1381-2019

Selz, V., K. E. Lowry, K. M. Lewis, H. L. Joy-Warren, W. van de Poll, S. Nirmel, A. Tong, and K. R. Arrigo. 2018. Distribution of *Phaeocystis antarctica*-dominated sea ice algal communities and their potential to seed phytoplankton across the western Antarctic Peninsula in spring. Mar. Ecol. Prog. Ser. **586**: 91–112.

Sloughter, T. M., N. S. Banas, and R. N. Sambrotto. 2019. Seasonal variation in light response of polar phytoplankton. J. Mar. Syst. **191**: 64–75. doi:10.1016/j.jmarsys.2018.12.003

Stammerjohn, S. E., D. G. Martinson, R. C. Smith, and R. A. Iannuzzi. 2008. Sea ice in the western Antarctic Peninsula region: Spatio-temporal variability from ecological and climate change perspectives. Deep Sea Res. II Top. Stud. Oceanogr. **55**: 2041–2058. doi:10.1016/j.dsr2.2008.04.026

Stoecker, D., D. Gustafson, C. Baier, and M. Black. 2000. Primary production in the upper sea ice. Aquat. Microb. Ecol. **21**: 275–287. doi:10.3354/ame021275

Strzepek, R. F., P. W. Boyd, and W. G. Sunda. 2019. Photosynthetic adaptation to low iron, light, and temperature in Southern Ocean phytoplankton. Proc. Nat. Acad. Sci. USA **116**: 4388–4393. doi:10.1073/pnas.1810886116

Tcherkez, G. G. B., G. D. Farquhar, and T. J. Andrews. 2006. Despite slow catalysis and confused substrate specificity, all ribulose bisphosphate carboxylases may be nearly perfectly optimized. Proc. Natl. Acad. Sci. USA **103**: 7246–7251. doi:10.1073/pnas.0600605103

UNESCO. 1994. Protocols for the Joint Global Ocean Flux Study (JGOFS) core measurements. *In* IOC manuals and guides, No. 29. UNESCO.

van Leeuwe, M. A., M. Fenton, E. Davey, J. M. Rintala, E. M. Jones, M. P. Meredith, and J. Stefels. 2022. On the phenology and seeding potential of sea-ice microalgal species. Elem. Sci. Anth. **10**: 00029. doi:10.1525/elementa.2021.00029

Wu, M., J. S. P. McCain, E. Rowland, R. Middag, M. Sandgren, A. E. Allen, and E. M. Bertrand. 2019. Manganese and iron deficiency in Southern Ocean *Phaeocystis antarctica* populations revealed through taxon-specific protein indicators. Nat. Commun. **10**: 3582. doi:10.1038/s41467-019-11426-z

Young, J. N. 2023*a*. Physical profiles of temperature, salinity, and brine volume in sea ice from samples collected on R/V Nathaniel B. Palmer cruise NBP1910 along the Western Antarctic Peninsula from November to December 2019. Biological and Chemical Oceanography Data Management Office (BCO-DMO). (Version 1) Version Date 2023-10-23. doi:10.26008/1912/bco-dmo.913655.1

Young, J. N. 2023*b*. Photosynthetic pigments from sea ice samples collected on R/V Nathaniel B. Palmer cruise NBP1910 along the Western Antarctic Peninsula from November to December 2019. Biological and Chemical Oceanography Data Management Office (BCO-DMO). (Version 1) Version Date 2023-10-17. doi:10.26008/1912/bco-dmo.913222.1

Young, J. N., J. A. L. Goldman, S. A. Kranz, P. D. Tortell, and F. M. M. Morel. 2015. Slow carboxylation of Rubisco constrains the rate of carbon fixation during Antarctic phytoplankton blooms. New Phytol. **205**: 172–181. doi:10.1111/nph.13021

Young, J. N., A. M. C. Heureux, R. E. Sharwood, R. E. M. Rickaby, F. M. M. Morel, and S. M. Whitney. 2016. Large variation in the Rubisco kinetics of diatoms reveals diversity among their carbon-concentrating mechanisms. J. Exp. Bot. **67**: 3445–3456. doi:10.1093/jxb/erw163

Zhu, Y., J. Ishizaka, S. C. Tripathy, S. Wang, C. Sukigara, J. Goes, T. Matsuno, and D. J. Suggett. 2017. Relationship between light, community composition and the electron requirement for carbon fixation in natural phytoplankton. Mar. Ecol. Prog. Ser. **580**: 83–100.

Acknowledgements

J.Y. was funded by the Simons Foundation Award 561645 and Alfred P. Sloan Foundation Fellowship. J.Y., J.W.D., H.D., and S.D.C. were funded by NSF Polar Programs OP 17445, S.R. was funded by NSF Graduate Research Fellowships Program. Rubisco measurements were supported by an NSERC Discovery Grant RGPIN-2015-05009 and Simons Foundation Grant 504183 to E.B. T.R.K. was supported by the Council for Scientific and Industrial Research (CSIR) in South Africa, Parliamentary Grant and the South African Department of Science and Innovation. We thank Hanis Zulumuthi and Megan Roberts for preparing Fig. 1 and Supplementary Fig. S1, respectively.

Conflict of Interest

None declared.

Submitted 23 April 2023
Revised 02 November 2023
Accepted 12 May 2024

Associate editor: Katherina Petrou